Nonlinear evolution of the MHD Kelvin-Helmholtz instability in a compressible plasma

S. H. Lai and L. H. Lyu

Institute of Space Science, National Central University, Chung-Li, Taiwan

Received 6 August 2004; revised 3 November 2005; accepted 9 November 2005; published 14 January 2006.

[1] Kelvin-Helmholtz (K-H) instability at a magnetohydrodynamic (MHD) tangential discontinuity (TD) is studied by means of two-dimensional MHD simulation. The TD is of finite thickness with both magnetic shear and velocity shear across the TD. Our simulation results indicate that the nonlinear evolution of MHD surface waves at the TD depends on the fast-mode Mach numbers of the plasma flows on two sides of the TD in the surface wave rest frame. When the fast-mode Mach numbers on both sides of the TD are less than 1, the K-H instability can grow into vortices or kink-type surface waves, depending on the orientation of the ambient magnetic field and the plasma beta. When the fast-mode Mach number on either side of the TD is greater than 1, nonlinear fast-mode plane waves are developed from the ridges of the surface waves and extended distance from the TD. A theoretical model based on the fast magnetosonic Mach cone formation is proposed to explain the formation of these nonlinear plane waves. The Mach angle of the fast magnetosonic Mach cone as a function of Mach number, orientation of ambient magnetic field, and plasma beta is derived. The flaring angles of these nonlinear plane waves measured from our simulation results are in good agreement with the Mach angles predicted by the theoretical model. Applications of our results to the Earth's magnetopause and to the solar wind are also discussed.

Citation: Lai, S. H., and L. H. Lyu (2006), Nonlinear evolution of the MHD Kelvin-Helmholtz instability in a compressible plasma, *J. Geophys. Res.*, *111*, A01202, doi:10.1029/2004JA010724.

1. Introduction

[2] Velocity shear in a fluid can trigger velocity-shear instability, which is also called the Kelvin-Helmholtz (K-H) instability. Examples of the K-H instability in nature include wind-induced water waves, vortices caused by water flows with different velocities in a river, cloud vortices generated by air flow around an island, and the wavy and twisting auroral curtain due to the shear motion of plasmas on two sides of an auroral arc. In addition to these visible wavy or vortex structures, large-scale phenomena are also observed by spacecraft in the velocity-shear regions of space plasma both at the flank magnetopause [e.g., *Ogilvie and Fitzenreiter*, 1989; *Chen and Kivelson*, 1993; *Chen et al.*, 1993; *Fairfield et al.*, 2000, 2003] and at the leading and trailing edges of high-speed solar wind streams [e.g., *Belcher and Davis*, 1971; *Mavromichalaki et al.*, 1988; *Neugebauer and Buti*, 1990].

[3] Nonlinear evolution of the K-H instability could result in vortices in saturation stage. However, owing to the tension force of water surface, the wind-induced water waves usually show undulate structures without vortices. Similarly, in the magnetohydrodynamic (MHD) plasma, when the background magnetic field is parallel or antiparallel to the sheared flows, the magnetic tension force can stabilize the instability and reduce the growth rate.

[4] The compressional effect in the K-H instability is negligible when the flow speeds on both sides of the TD are subsonic in the surface wave rest frame. The compressional effect becomes important when the flow speed on either side becomes supersonic or supermagnetosonic in the surface wave rest frame. Supermagnetosonic velocity shears are commonly observed in the solar wind [e.g., *Mavromichalaki et al.*, 1988; *Neugebauer and Buti*, 1990] and at the Earth's magnetopause [e.g., *Chen and Kivelson*, 1993]. Numerical modeling of the nonlinear evolution of the K-H instability in compressible MHD plasma can help us to understand further the underline processes of the formation of the nonlinear disturbances in the solar wind and at the Earth's magnetopause.

[5] K-H instabilities at the magnetopause and the low-latitude boundary layer have been studied extensively by numerical simulations in the past 20 years [e.g., *Miura*, 1982, 1984, 1987, 1990, 1992, 1997, 1999; *Wu*, 1986; *Manuel and Samson*, 1993; *Thomas and Winske*, 1993; *Otto and Fairfield*, 2000]. In this paper, we study the generation and evolution of the K-H instability in the MHD plasma by means of two-dimensional MHD simulations. We choose to perform our simulation in a system with an extremely long dimension along the direction normal to the velocity-shear layer. It will be shown later in section 3 that the extremely long dimension simulation is especially

0148-0227/06/2004JA010724$09.00

needed for studying nonlinear evolution of the fast-mode waves in supermagnetosonic K-H instabilities.

[6] The outlines of this paper are as follows. The basic equations and the simulation model are introduced in section 2. Simulation results are presented in section 3. A theoretical model based on Mach cone formation is proposed in section 4 to explain the formation of nonlinear plane waves in the high-Mach-number K-H instability. Discussions and summary are given in section 5.

2. Simulation Model

[7] Basic equations used in our two-dimensional MHD simulation are as follows:

$$\frac{\partial \rho}{\partial t} + \nabla \cdot (\rho \mathbf{V}) = 0 \tag{1}$$

$$\frac{\partial}{\partial t}(\rho \mathbf{V}) + \nabla \cdot \left[\rho \mathbf{V}\mathbf{V} + \left(p + \frac{B^2}{2\mu_0}\right)\mathbf{1} - \frac{\mathbf{B}\mathbf{B}}{\mu_0}\right] = 0 \tag{2}$$

$$\frac{\partial}{\partial t}\left(\frac{1}{2}\rho V^2 + \frac{3}{2}p + \frac{B^2}{2\mu_0}\right) + \nabla \cdot \left[\left(\frac{1}{2}\rho V^2 + \frac{5}{2}p + \frac{B^2}{\mu_0}\right)\mathbf{V} - \frac{\mathbf{B}(\mathbf{B}\cdot\mathbf{V})}{\mu_0}\right] = 0 \tag{3}$$

$$\frac{\partial \mathbf{B}}{\partial t} = \nabla \times (\mathbf{V} \times \mathbf{B}) \tag{4}$$

$$\nabla \cdot \mathbf{B} = 0, \tag{5}$$

where $\mathbf{B}$ is magnetic field and ρ, $\mathbf{V}$, and p are mass density, average velocity, and thermal pressure of plasma, respectively. MHD Ampere's law has been used to derive equation (2). MHD Ohm's law $\mathbf{E} + \mathbf{V} \times \mathbf{B} = 0$ has been used in equations (3) and (4). We use the second order Lax-Wendroff scheme [e.g., *Richtmyer and Morton*, 1967] to integrate equations (1)–(4) and to advance $\mathbf{B}$, ρ, $\mathbf{V}$, and p in time. In order to balance numerical instability, a small diffusion term is added in each of the equations (2)–(4). Alternating direction implicit (ADI) method [e.g., *Press et al.*, 1988] is used to include these diffusion terms numerically.

[8] We choose the initial background medium to be a velocity shear with a finite thickness across an MHD tangential discontinuity (TD). We use the following hyperbolic tangent function to setup background equilibrium states across the transition layer of the TD:

$$A_0(x) = \frac{A_{02} + A_{01}}{2} + \frac{A_{02} - A_{01}}{2}\tanh\left(\frac{x}{a}\right), \tag{6}$$

where a is proportional to the thickness of the transition layer. The variable $A_0(x)$ can be $\mathbf{V}_0(x)$, $\mathbf{B}_0(x)$ or $\rho_0(x)$. Subscripts "1" and "2" denote parameters on the left-hand side ($x < 0$) and the right-hand side ($x > 0$) of the TD, respectively. For convenience, the regions outside the transition layer with nearly uniform initial equilibrium fields will be called "region 1" for $x < 0$ and "region 2" for $x > 0$ in the rest of the paper. According to equation (6), the TD is located at $x = 0$ with gradients along the x direction. We assume that the background velocity is in the $\pm y$ direction, i.e., $\mathbf{V}_0(x) = V_{0y}(x)\hat{\mathbf{y}}$, the background magnetic field vector lies in the x-z plane, i.e., $\mathbf{B}_0(x) = B_{0y}(x)\hat{\mathbf{y}} + B_{0z}(x)\hat{\mathbf{z}}$, and all the variables are uniform in the z direction, i.e., $\nabla = \hat{\mathbf{x}}(\partial/\partial x) + \hat{\mathbf{y}}(\partial/\partial y)$. We define θ_{01} and θ_{02} to be the angles between the y-axis and the background magnetic fields $\mathbf{B}_{01}$ and $\mathbf{B}_{02}$, respectively, i.e., $B_{0y1} = B_{01}\cos\theta_{01}$, $B_{0z1} = B_{01}\sin\theta_{01}$, $B_{0y2} = B_{02}\cos\theta_{02}$, and $B_{0z2} = B_{02}\sin\theta_{02}$. The background thermal pressure $p_0(x)$ is chosen such that the sum of the thermal pressure and the magnetic pressure is uniform in the x direction, i.e.,

$$p_0(x) = p_{01} + B_{01}^2/2\mu_0 - \left[B_{0y}^2(x) + B_{0z}^2(x)\right]/2\mu_0, \tag{7}$$

where $B_{0y}(x)$ and $B_{0z}(x)$ can be obtained from equation (6).

[9] Since $\tanh(1.5) \approx 0.9$, we define $W = 3a$ to be the thickness of the transition layer, which is also chosen to be the normalization length in our discussion. The size of the simulation box is $L_x \times L_y$. We impose a uniform boundary condition ($\partial/\partial x = 0$) at $x = \pm L_x/2$ and a periodic boundary condition at $y = \pm L_y/2$.

[10] To trigger the K-H instability, an initial velocity perturbation $\delta\mathbf{v} = \delta v_x(x,y)\hat{\mathbf{x}} + \delta v_y(x,y)\hat{\mathbf{y}}$, which satisfies $\nabla \cdot \delta\mathbf{v} = 0$, is added to the transition layer.

[11] The initial perturbation is given in the following from

$$\delta v_x(x,y) = -\delta v_0 \mathrm{sech}\left(\frac{x}{a_x}\right)\sin\left(\frac{2\pi y}{\lambda_y}\right) \tag{8}$$

$$\delta v_y(x,y) = \delta v_0 \frac{\lambda_y}{2\pi a_x}\mathrm{sech}\left(\frac{x}{a_x}\right)\tanh\left(\frac{x}{a_x}\right)\cos\left(\frac{2\pi y}{\lambda_y}\right). \tag{9}$$

As we can see that the initial perturbation is periodic in the y direction, with wavelength equal to λ_y, but finite extent in the x-direction around $x = 0$, from where the perturbation amplitude decays exponentially with a spatial decay length equal to a_x.

[12] In this study, we use the following method to determine the occurrence of the K-H instability and the time when the K-H instability reaches a saturation stage. We choose a field variable (A), which is uniform in an equilibrium state (A_0) but has significant variations ($\delta A = A - A_0$) after the initial disturbance. We calculate the maximum of δA^2 (which will be denoted by $\delta A^2_{\max}$) for the entire simulation domain at each simulation time step. We then plot the resulting time series of $\delta A^2_{\max}$ in a logarithmic scale. The K-H instability is considered to take place if $\delta A^2_{\max}$ of one of the field variables changes more than 10^2 from its initial value. After a stable growth phase, a numerical stable simulation should reach a saturation stage and we should be able to determine the saturation stage from the logarithmic plots of $\delta A^2_{\max}$. Possible field variables that can be used to determine the saturation stage include the x component and the z component of the velocity field (V_x and V_z), the x component of the magnetic field (B_x), or the density ρ (if $\rho_{01} = \rho_{02}$).

3. Simulation Results

[13] To find out what controls the nonlinear evolution of the K-H instability, we studied more than 40 cases. Twenty of them are listed in Tables 1 and 2.

Table 1. Background Equilibrium Fields and Simulation Results

Case	Background Equilibrium Fields									Simulation Results		
	$\frac{\rho_{01}}{\rho_a}$	$\frac{\rho_{02}}{\rho_a}$	$\frac{V_{0y1}}{V_a}$	$\frac{V_{0y2}}{V_a}$	$\frac{p_{01}}{p_a}$	$\frac{B_{01}}{B_a}$	$\frac{B_{02}}{B_a}$	θ_{01}	θ_{02}	M_{F0y1}	M_{F0y2}	Type
1	1	1	0	1.700	0.5	1.5811	1.4142	90°	90°	0.4977	0.5050	V
2	1	1	0	1.425	2	0.5000	0.5477	0°	0°	0.5519	0.5589	K
3	1	1	0	2.850	2	0.7071	1.2910	90°	90°	0.8390	1.0510	PK
4	1	1	0	2.565	2	0.7071	1.2910	0°	0°	0.8095	1.1774	PK
5	1	1	0	5.700	2	0.7071	1.2910	0°	0°	0.9567	3.4587	PK
6	1	1	0	1.900	2	0.5000	0.5477	0°	0°	0.7359	0.7452	K
7	1	1	0	1.710	2	0.5774	0.8165	0°	0°	0.6623	0.7255	K
8	1	1	0	2.185	2	0.7071	1.2910	30°	30°	0.5979	0.9979	PK
9	1	1	0	2.850	2	0.7071	1.2910	30°	30°	0.8441	1.2384	PK
10	1	1	0	1.425	2	0.5774	0.8165	30°	30°	0.5365	0.5582	K
11	1	1	0	1.425	2	0.7071	1.2910	70°	70°	0.4893	0.4696	V
12	1	1	0	2.850	2	1.1547	0.8165	75°	75°	0.8297	0.8435	V
13	1	1	3.0	0	2	0.7071	1.2910	75°	75°	1.1038	0.8095	PK
14	1	0.01	5.0	0	2	1.0000	1.6514	90°	90°	1.5922	0.1396	PK
15	1	0.01	2.0	0	2	1.0000	1.6514	90°	90°	0.6124	0.0582	V
16	1	1	0	1.425	2	0.5000	0.5000	85°	45°	0.5149	0.5309	V
17	1	1	0	1.425	2	1.0000	1.0000	85°	45°	0.4367	0.4693	K
18	1	1	0	3.040	2	0.8032	0.9390	85°	45°	0.7503	1.3327	PK
19	1	1	0	1.425	2	0.5000	0.5000	90°	0°	0.5146	0.5519	V
20	1	1	0	1.425	2	0.7071	0.7071	0°	90°	0.5519	0.4840	K

[14] Table 1 lists the normalized background equilibrium fields and the simulation results for the 20 cases. The normalization constants V_a, B_a, ρ_a, and p_a used in Tables 1 and 2 satisfy the following relations: $V_a = B_a/\sqrt{\mu_0\rho_a}$ and $p_a = B_a^2/2\mu_0$. A system with dimension $L_x \times L_y = 100W \times 50W$, grid size $\Delta_x = \Delta_y = 0.25W$, and initial perturbation with $a_x = 0.33W$, $\lambda_y = 12.5W$, and $\delta v_0 \approx 0.01|V_{0y1} - V_{0y2}|$ are chosen. Before discussing the simulation results listed in Table 1, we will first introduce the characteristic speeds listed in Table 2.

[15] We first measure U_t from our simulation results, where U_t is the y-component of the surface-wave phase velocity observed in the simulation rest frame. It is found that U_t is not exactly equal to $(V_{0y1} + V_{0y2})/2$, particularly for the supermagnetosonic cases. The relative speeds $U_t - V_{0y1}$ and $U_t - V_{0y2}$ listed in Table 2 are the speeds of the surface waves observed in the plasma rest frames of region 1 ($x < 0$) and region 2 ($x > 0$), respectively. The characteristic speeds C_{I0y1}, C_{I0y2}, C_{F0y1}, and C_{F0y2} listed in Table 2 are defined as follows:

$$C_{I0y1} = B_{0y1}/\sqrt{\mu_0\rho_{01}} \tag{10}$$

$$C_{I0y2} = B_{0y2}/\sqrt{\mu_0\rho_{02}} \tag{11}$$

$$C_{F0y1}^2 = \frac{1}{2}\left\{C_{A01}^2 + C_{S01}^2 + \sqrt{\left(C_{A01}^2 + C_{S01}^2\right)^2 - 4C_{A01}^2 C_{S01}^2 \cos^2\theta_{01}}\right\} \tag{12}$$

$$C_{F0y2}^2 = \frac{1}{2}\left\{C_{A02}^2 + C_{S02}^2 + \sqrt{\left(C_{A02}^2 + C_{S02}^2\right)^2 - 4C_{A02}^2 C_{S02}^2 \cos^2\theta_{02}}\right\} \tag{13}$$

Table 2. Characteristic Speeds Measured From Simulation Results

Case	$\frac{U_t}{V_a}$	$\frac{U_t - V_{0y1}}{V_a}$	$\frac{U_t - V_{0y2}}{V_a}$	$\frac{C_{I0y1}}{V_a}$	$\frac{C_{I0y2}}{V_a}$	$\frac{C_{F0y1}}{V_a}$	$\frac{C_{F0y2}}{V_a}$
1	0.8500	0.8500	−0.8500	0	0	1.7078	1.6833
2	0.7125	0.7125	−0.7125	0.4999	0.5477	1.2910	1.2747
3	1.2350	1.2350	−1.6150	0	0	1.4719	1.5366
4	1.0450	1.0450	−1.5200	0.7071	1.2910	1.2910	1.2910
5	1.2350	1.2350	−4.4650	0.7071	1.2910	1.2910	1.2910
6	0.9500	0.9500	−0.9500	0.4999	0.5477	1.2910	1.2747
7	0.8550	0.8550	−0.8550	0.5773	0.8165	1.2910	1.1785
8	0.8075	0.8075	−1.3775	0.6124	1.1179	1.3505	1.3804
9	1.1400	1.1400	−1.7100	0.6124	1.1179	1.3505	1.3804
10	0.7125	0.7125	−0.7125	0.4999	0.7071	1.3281	1.2764
11	0.7125	0.7125	−0.7125	0.2418	0.4415	1.4563	1.5173
12	1.4250	1.4250	−1.4250	0.2989	0.2113	1.7174	1.6894
13	1.2350	−1.6150	1.2350	0.1830	0.3341	1.4631	1.5257
14	2.4	−2.6	2.4	0	0	1.6330	17.1890
15	1.0	−1.0	1.0	0	0	1.6330	17.1890
16	0.7125	0.7125	−0.7125	0.0436	0.3536	1.3839	1.3420
17	0.7125	0.7125	−0.7125	0.0871	0.7071	1.6315	1.5183
18	1.1400	1.1400	−1.9000	0.0700	0.6640	1.5193	1.4257
19	0.7125	0.7125	−0.7125	0	0.4999	1.3844	1.2910
20	0.7125	0.7125	−0.7125	0.7071	0	1.2910	1.4719

where $C_{A01}^2 = B_{01}^2/\mu_0\rho_{01}$, $C_{A02}^2 = B_{02}^2/\mu_0\rho_{02}$, $C_{S01}^2 = 5p_{01}/3\rho_{01}$, and $C_{S02}^2 = 5p_{02}/3\rho_{02}$. Namely, the characteristic speeds C_{I0y1}, C_{I0y2}, C_{F0y1}, and C_{F0y2} are the phase speeds of the MHD intermediate-mode and fast-mode waves in region 1 ($x < 0$) and region 2 ($x > 0$) with the wave numbers $\mathbf{k}$ along the surface wave propagation direction ($\mathbf{y}$).

[16] The simulation results shown in Table 2 are exclusively for $|U_t - V_{0y1}| > C_{I0y1}$ and $|U_t - V_{0y2}| > C_{I0y2}$. Actually, no K-H instability can be found if the total velocity shear $|V_{0y2} - V_{0y1}|$ is less than $C_{I0y1} + C_{I0y2}$. These results are consistent with previous theoretical predictions [*Chandrasekhar*, 1961; *Miura and Pritchett*, 1982].

[17] The fast-mode Mach numbers of the surface waves listed in Table 1 are defined by

$$M_{F0y1}^2 = \left(U_t - V_{0y1}\right)^2 / C_{F0y1}^2 \tag{14}$$

and

$$M_{F0y2}^2 = \left(U_t - V_{0y2}\right)^2 / C_{F0y2}^2. \tag{15}$$

[18] Table 1 lists the following three types of nonlinear K-H instabilities found in the simulations: (1) vortex-type nonlinear K-H instability (V), which is characterized by large-scale whirling structures across the transition layer; (2) nonlinear K-H instability with kink-type surface wave (K), which is characterized by a undulate surface wave with possible eddies on two sides of the transition layer; and (3) nonlinear K-H instability with combination of plane waves and kink-type surface wave (PK), but without large-scale whirling structures across the transition layer. Examples of the three types of K-H instabilities are shown in Figures 1–4.

[19] Figure 1 shows the simulation results of Case 1. The top two panels are gray-level plots of the normalized plasma density $\rho(x,y)/\rho_a$ and the normalized magnetic field strength $B(x,y)/B_a$ at a saturation stage $t = 37.5\tau_a$, where $\tau_a = W/V_a$. The lower panel shows the temporal variation of $\log_{10}(\delta\rho_{\max}^2/\rho_a^2)$. The input parameters of Case 1 are given in Table 1. According to Table 1, Case 1 is characterized by $\theta_{01} = \theta_{02} = 90°$, $M_{F0y1} < 1$, and $M_{F0y2} < 1$. In this case, the initial surface disturbance first amplified into a nonlinear undulate surface wave and then developed into vortex structures. The vortex structure can whirl across the transition layer to rotate plasmas with field lines on two sides of the TD in the two-dimensional (2-D) simulation with $\theta_{01} = \theta_{02} = 90°$. The vortex structures shown in Figure 1 are similar to the results obtained in previous simulation studies [e.g., *Miura and Pritchett*, 1982; *Miura*, 1987, 1992].

[20] Figure 2 shows the simulation results of Case 2. The top two panels are gray-level plots of the normalized plasma density $\rho(x,y)/\rho_a$ and the normalized magnetic field strength $B(x,y)/B_a$ at a saturation stage $t = 87.5\tau_a$. The lower panel shows the temporal variation of $\log_{10}(\delta\rho_{\max}^2/\rho_a^2)$. According to Table 1, Case 2 is characterized by $\theta_{01} = \theta_{02} = 0°$, $M_{F0y1} < 1$, and $M_{F0y2} < 1$. The time to reach the saturation stage in Case 2 is much longer than the time in Case 1. Large-scale whirling structures across the transition layer cannot be found in this case. Localized and intermittent high-speed tangential plasma flows can be found inside the wavy transition layer in a gray-level plot of field $V_y(x,y)$ (not shown), which may indicate transient magnetic reconfiguration in this region. Localized magnetic reconnection inside the transition layer has been reported in previous MHD simulations by *Otto and Fairfield* [2000]. Without sufficient dissipation in our simulation code, it would be hard for magnetic reconnection to occur in our simulation. However, even without magnetic reconnection, we expect that the magnetic tension force alone could result in transient magnetic reconfiguration in the transition layer to prevent formation of large-scale vortex structures across the transition layer in Case 2.

[21] Note that the absence of vortex structure in Case 2 does not mean that the vorticity, $\Omega_z\hat{\mathbf{z}} = \nabla \times \mathbf{V}$, vanishes in Case 2. Figure 3 shows the distributions of the normalized vorticity ($\Omega_z\,\tau_a$) at the saturation stages of Case 1 (top) and Case 2 (bottom). The strong vorticities coincide with the vortex structures in Case 1. The strong vorticities are concentrated in the narrow regions on the two sides of the undulant transition layer in Case 2. According to the velocity distributions listed in Table 1, the initial vorticity in Case 2 is slightly smaller than it in Case 1. Owing to insufficient dissipation in our simulation code, the circulation, $\Gamma = \oint \mathbf{V} \cdot d\mathbf{l} = \int\int \Omega_z dxdy$, is nearly invariant in our simulation, which makes the peak of vorticity in Case 2 much greater than it in Case 1 at the saturation stage of the K-H instability.

[22] Figure 4 shows the simulation results of Case 3. The top two panels are gray-level plots of the normalized plasma density $\rho(x,y)/\rho_a$ and the normalized magnetic field strength $B(x,y)/B_a$ at a saturation stage $t = 37.5\tau_a$. The lower panel shows the temporal variation of $\log_{10}(\delta\rho_{\max}^2/\rho_a^2)$. According to Table 1, Case 3 is characterized by $\theta_{01} = \theta_{02} = 90°$, $M_{F0y1} < 1$, and $M_{F0y2} > 1$. Nonlinear plane waves can be found in region 2 ($x > 0$), where the fast-mode Mach number M_{F0y2} is greater than 1. The strong vorticity is confined in the undulate transition layer (not shown). No cross-transition-layer vortex structures can be found in Case 3.

[23] Figure 5 shows the simulation results of Case 4. The top two panels are gray-level plots of the normalized plasma density $\rho(x,y)/\rho_a$ and the normalized magnetic field strength $B(x,y)/B_a$ at a saturation stage $t = 75\tau_a$. The lower panel shows the temporal variation of $\log_{10}(\delta\rho_{\max}^2/\rho_a^2)$. The maximum change on $\log_{10}(\delta\rho_{\max}^2/\rho_a^2)$ is less than 2 but the maximum change on $\log_{10}(\delta B_{x\ \max}^2/B_a^2)$ is greater than 2 (not shown) in this case. The time to reach the saturation stage in Case 4 is much longer than the time in Case 3. According to Table 1, Case 4 is characterized by $\theta_{01} = \theta_{02} = 0°$, $M_{F0y1} < 1$, and $M_{F0y2} > 1$. Again, no cross-transition-layer vortex structures can be found in Case 4. The strong vorticity is also concentrated in the undulate transition layer in this case (not shown). Nonlinear plane waves can be found in region 2 ($x > 0$), where the fast-mode Mach number of the plasma flow in the surface wave rest frame is greater than 1.

[24] Simulation results of the 40 cases studied including those listed in Table 1 are summarized in Figure 6. Figure 6 shows the Mach-numbers dependence of our simulations. Nonlinear plane waves can be found in the saturation stages when one of the Mach numbers M_{F0y1} or M_{F0y2} is equal or

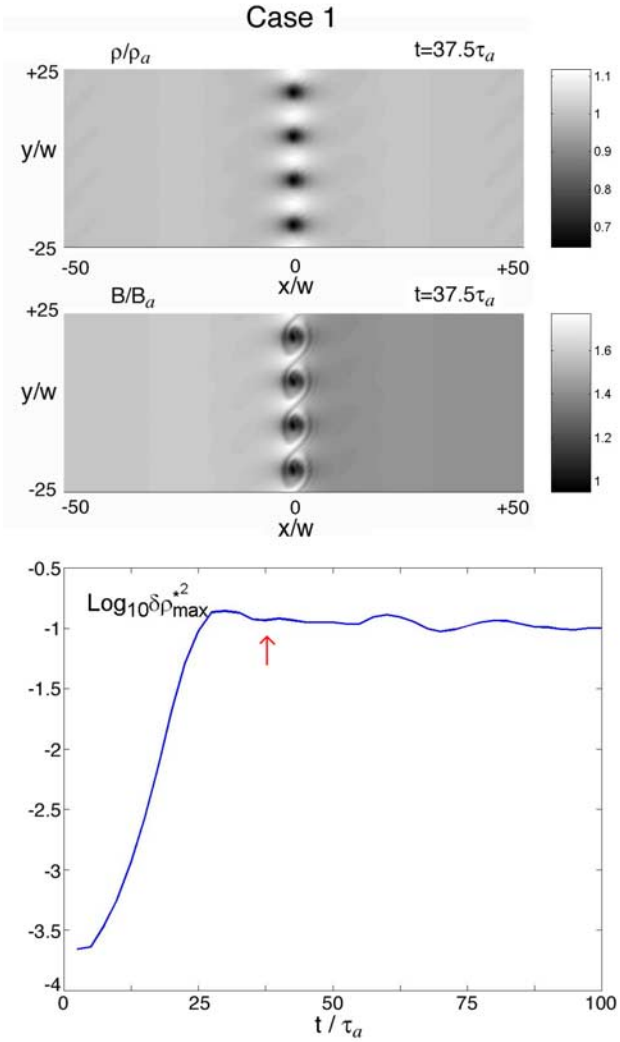

Figure 1. Simulation results of Case 1. The top two panels are gray-level plots of the normalized plasma density $\rho(x,y)/\rho_a$ and the normalized magnetic field strength $B(x,y)/B_a$ at a saturation stage $t = 37.5\tau_a$. The lower panel shows the temporal variation of $\log_{10}(\delta\rho^2_{max}/\rho^2_a)$. This is an example of nonlinear K-H instability with cross-transition-layer vortex structures formed in the saturation stage. According to Table 1, both M_{F0y1} and M_{F0y2} are less than 1 in the Case 1. The background magnetic fields on both sides of the TD are in the z direction.

greater than 1. No plane waves but vortex-type or kink-type surface waves can be found in the saturation stages if both M_{F0y1} and M_{F0y2} are less than 1.

[25] Figure 7 shows the distribution of vortex-type and kink-type surface waves as a function of θ_{01} and θ_{02} for the cases with the Mach numbers, M_{F0y1} and M_{F0y2}, less than 1. Vortex-type surface waves can be found only if θ_{01} or θ_{02} is greater than a critical angle, which is 70° for all the cases we studied. However, we expect that the critical angle should depend on the plasma beta. The critical angle should decrease with increasing plasma beta. Since it requires more samples to determine the critical angle distribution in the (θ_{01}, θ_{02}, β_{01}, β_{02}) space, the study of critical angle distribution is beyond the scope of this paper.

4. On the Formation of Nonlinear Plane Waves

[26] The strong Mach-number dependence shown in Figure 6 provides useful information that helps us to identify the cause of the nonlinear plane waves in the simulation. We propose that the formation of these nonlinear waves is similar to the formation of the sonic Mach cone in gas dynamics.

[27] Figure 8 illustrates the formation of the sonic/magnetosonic Mach cone when a point source moves superson-

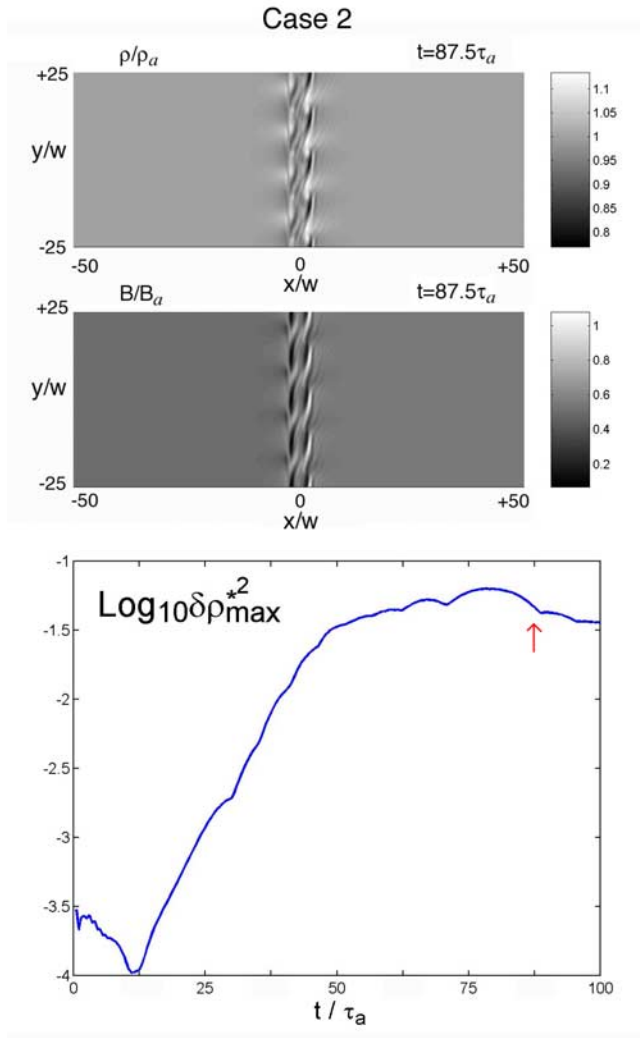

Figure 2. Simulation results of Case 2. The top two panels are gray-level plots of the normalized plasma density $\rho(x,y)/\rho_a$ and the normalized magnetic field strength $B(x,y)/B_a$ at a saturation stage $t = 87.5\tau_a$. The lower panel shows the temporal variation of $\log_{10}(\delta\rho^2_{max}/\rho^2_a)$. This is an example of nonlinear K-H instability with kink-type surface wave but without cross-transition-layer vortices in the saturation stage. According to Table 1, both M_{F0y1} and M_{F0y2} are less than 1 in the Case 2. The background magnetic fields on both sides of the TD are in the y direction.

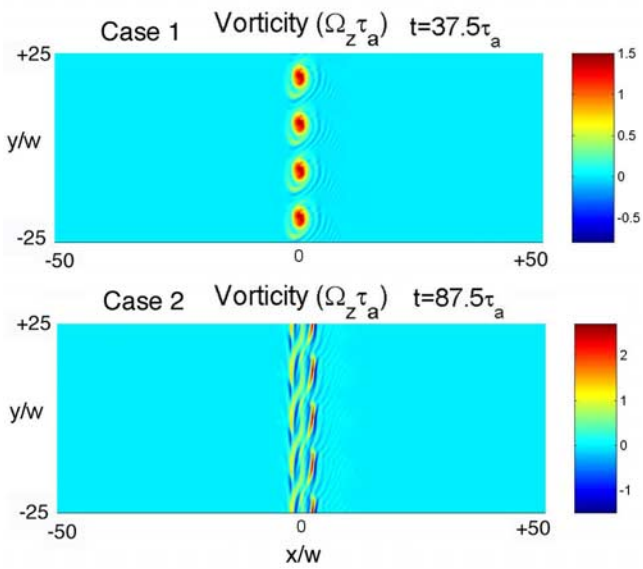

Figure 3. The distributions of the normalized vorticity ($\Omega_z \tau_a$) at the saturation stages of (top) Case 1 and (bottom) Case 2. See the text for the detail discussion on the vorticity distributions in these two cases.

ically/supermagnetosonically with respect to the background gas/plasma. Figure 8a shows a sketch of the formation of the sonic Mach cone. The sonic Mach cone is a surface of strong constructive interference of sound waves emitted from a point source that moved supersonically with respect to the ambient gas. The half-cone angle α, which is also called Mach angle, is a function of the Mach number of the point source. If the speed of the point source relative to the background medium is equal to $V_S = M_S C_S$, then we have $sb = V_S \Delta t = M_S C_S \Delta t$ and $sc = C_S \Delta t$, where C_S is the sound speed, $M_S \geq 1$ is the sound Mach number of the point source, sb is the distance between point s and point b, and sc is the distance between point s and point c. Thus the Mach angle of the sonic Mach cone can be determined by

$$\alpha = \sin^{-1}(1/M_S). \tag{16}$$

[28] If the nonlinear steepening of the constructive interference surface forms a shock, the nonlinear waves should move slightly faster than the one shown in Figure 8a. In that case, the actual Mach angle will be slightly greater than the one estimated in equation (16).

[29] The simple relation between the Mach number and the Mach angle can be found only in uniform gas dynamics, where the phase velocity and the group velocity of sound waves are isotropic and are identical to each other. In MHD plasma, the group velocity and the phase velocity of the fast magnetosonic wave are not isotropic and, in general, are not identical to each other. As a result, the fast magnetosonic Mach cone in MHD plasma may not be axially symmetric. We will show in this section that the Mach angle (i.e., the half-cone angle) in MHD plasma depends not only on the Mach number but also on the orientation of the ambient magnetic field and the plasma beta of the background medium.

[30] Figure 8b shows the cross section of the fast magnetosonic Mach cone in the plane where a point source moves supermagnetosonically parallel to the ambient magnetic field. We use a coordinate system such that the point source moves in the $-y$ direction to where the ambient magnetic field is pointing. It is shown that the fast-mode waves emitted from a point source form closed surfaces that expand outward in the group velocity of the fast-mode waves. The shape of these closed surfaces is close to spheres but with shorter radii along the magnetic field direction.

[31] The fast magnetosonic Mach cone in Figure 8b is tangent to the largest closed surface at point g. The vector sg is along the group velocity of the fast magnetosonic wave,

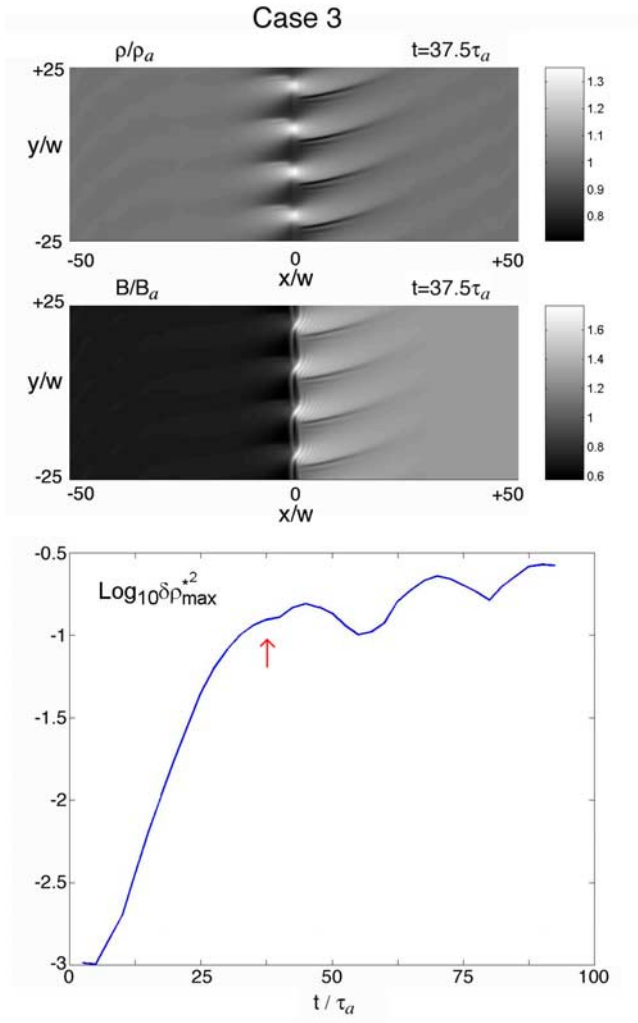

Figure 4. Simulation results of Case 3. The top two panels are gray-level plots of the normalized plasma density $\rho(x,y)/\rho_a$ and the normalized magnetic field strength $B(x,y)/B_a$ at a saturation stage $t = 37.5\tau_a$. The lower panel shows the temporal variation of $\log_{10}(\delta\rho_{max}{}^2/\rho_a{}^2)$. This is an example of nonlinear K-H instability with kink-type surface wave at $x = 0$ and nonlinear plane waves in region 2 ($x > 0$) in the saturation stage. According to Table 1, Case 3 is characterized by $M_{F0y1} < 1$ and $M_{F0y2} > 1$. In this case, the background magnetic fields on both sides of the TD are in the z direction.

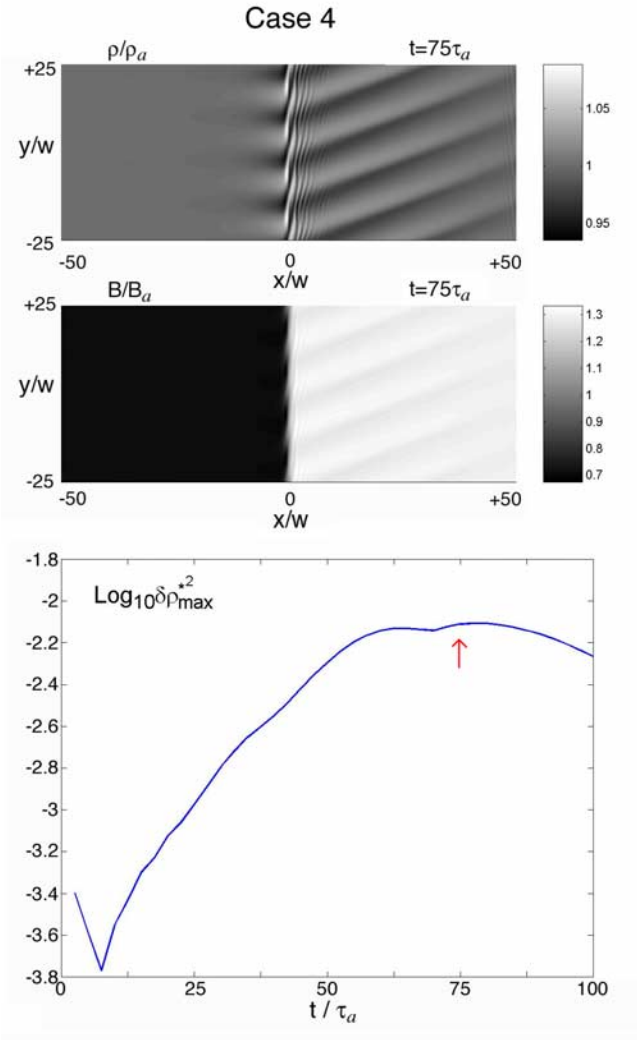

Figure 5. Simulation results of Case 4. The top two panels are gray-level plots of the normalized plasma density $\rho(x,y)/\rho_a$ and the normalized magnetic field strength $B(x,y)/B_a$ at a saturation stage $t = 75\tau_a$. The lower panel shows the temporal variation of $\log_{10}(\delta\rho^2_{\max}/\rho_a^2)$. This is another example of nonlinear K-H instability with kink-type surface wave at $x = 0$ and nonlinear plane waves in region 2 ($x > 0$) in the saturation stage. According to Table 1, Case 4 is characterized by $M_{F0y1} < 1$ and $M_{F0y2} > 1$. In this case, the background magnetic fields on both sides of the TD are in the y direction.

whereas the vector sc is along the corresponding phase velocity. It is shown that the vector sc is perpendicular to the magnetosonic Mach cone. The Mach angle α of the magnetosonic Mach cone shown in Figure 8b depends on the angle ψ, which is the angle between vectors sc and sb. Let us assume that the point source is moving at speed $V_S = M_{F0y}C_{F0y}$, where C_{F0y} is the phase speed of the fast-mode wave propagating along the y-axis and M_{F0y} is the fast-mode Mach number of the point source. The length of each vector shown in Figure 8b satisfies $sb = V_S\Delta t = M_{F0y}C_{F0y}\Delta t$, $sc = C_{F0\psi}\Delta t$, and $sg = C_{gF0\psi}\Delta t$, where $C_{F0\psi}$ is the phase speed of fast-mode wave propagating along the direction of vector sc and $C_{gF0\psi}$ is the corresponding group speed. Since sc is perpendicular to bc in Figure 8b, we have $\cos\psi = \sin\alpha$ and the Mach angle α satisfies

$$\sin^2\alpha = \frac{C^2_{F0\psi}}{M^2_{F0y}C^2_{F0y}} = \frac{\frac{1}{2}\left\{C^2_{A0} + C^2_{S0} + \sqrt{\left(C^2_{A0} + C^2_{S0}\right)^2 - 4C^2_{A0}C^2_{S0}\cos^2\psi}\right\}}{M^2_{F0y}C^2_{F0y}}. \tag{17}$$

Substituting $\cos\psi = \sin\alpha$ into equation (17) yields

$$\sin^2\alpha = \frac{C^2_{S0} + C^2_{A0}}{M^2_{F0y}C^2_{F0y}} - \frac{C^2_{S0}C^2_{A0}}{M^4_{F0y}C^4_{F0y}} \tag{18}$$

or

$$\alpha = \sin^{-1}\sqrt{\frac{C^2_{S0} + C^2_{A0}}{M^2_{F0y}C^2_{F0y}} - \frac{C^2_{S0}C^2_{A0}}{M^4_{F0y}C^4_{F0y}}}. \tag{19}$$

[32] Figure 8c shows two cross sections of the fast magnetosonic Mach cone when a point source moves supermagnetosonically perpendicular to the ambient magnetic field. We use a coordinate system such that the point source moves in the $-y$ direction and the ambient magnetic field is along the z axis. In this case, the fast magnetosonic Mach cone is not axially symmetric. The fast magnetosonic Mach cone in Figure 8c has the maximum Mach angle $\alpha_{\max}$ in the xy-plane, i.e.,

$$\alpha_{\max} = \sin^{-1}\left(1/M_{F0y}\right). \tag{20}$$

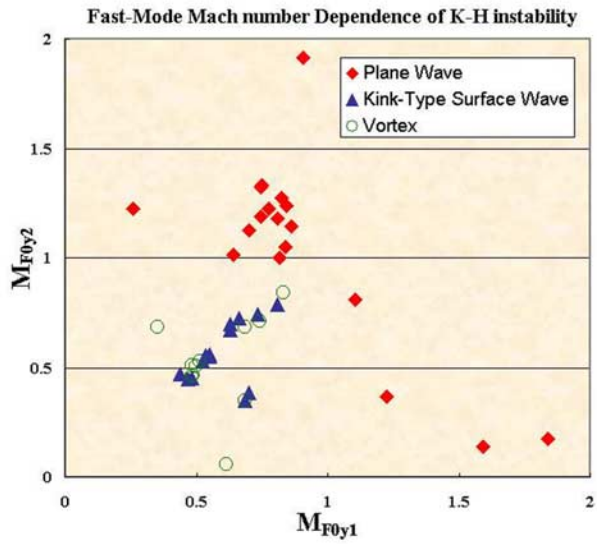

Figure 6. Scatter plot of nonlinear waves found in the saturation stage of the K-H instability on the M_{F0y1}-M_{F0y2} plane. Nonlinear plane wave structures (solid square) can be found in the saturation stage when one of the Mach numbers M_{F0y1} or M_{F0y2} is greater than or equal to 1. No plane waves but cross-transition-layer vortex structures (open circle) or kink-type surface waves without cross-transition-layer vortices (solid triangle) can be found in the saturation stage if both M_{F0y1} and M_{F0y2} are less than 1.

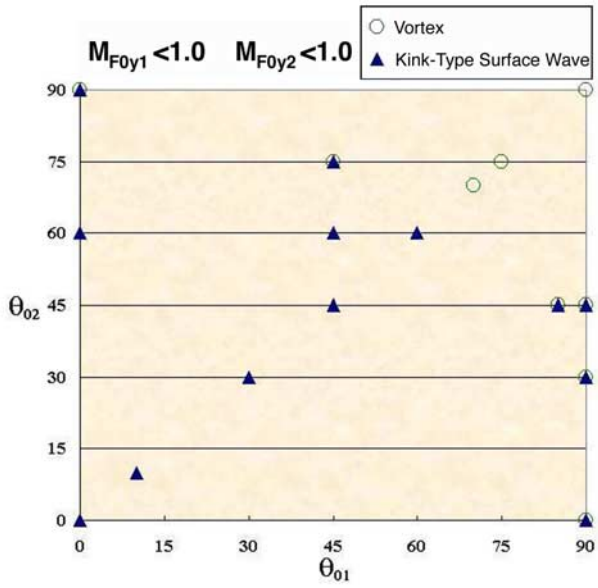

Figure 7. Scatter plot of nonlinear waves found at the saturation stage of low-Mach-number K-H instability on the θ_{01}-θ_{02} plane. Only simulation results with $M_{F0y1} < 1$ and $M_{F0y2} < 1$ are shown. The open circles denote nonlinear vortex-type K-H instabilities with cross-transition-layer vortex structures in the saturation stage. The solid triangles denote nonlinear K-H instabilities with kink-type surface waves and possible eddy structures on two sides of the surface wave but without cross-transition-layer vortices in the saturation stage. The nonlinear vortex-type K-H instabilities can be found only if θ_{01} or θ_{02} is greater than a critical angle, which is 70° for all the cases we studied. However, we expect that the critical angle should depend on the plasma beta. The critical angle should decrease with increasing plasma beta. Since it requires more samples to determine the critical angle distribution in the $(\theta_{01}, \theta_{02}, \beta_{01}, \beta_{02})$ space, the study of critical angle distribution is beyond the scope of this paper.

[33] The fast magnetosonic Mach cone in Figure 8c has the minimum Mach angle $\alpha_{\min}$ in the yz-plane. Let ψ be the acute angle between the ambient magnetic field and the normal vector of the fast magnetosonic Mach cone in the yz-plane. The angle ψ is equal to the Mach angle $\alpha_{\min}$. Thus the Mach angle $\alpha_{\min}$ in the yz-plane can be obtained by solving the following equation:

$$\sin^2\alpha_{\min} = \frac{C_{F0\psi}^2}{M_{F0y}^2 C_{F0y}^2} = \frac{\frac{1}{2}\left\{C_{A0}^2 + C_{S0}^2 + \sqrt{\left(C_{A0}^2 + C_{S0}^2\right)^2 - 4C_{A0}^2 C_{S0}^2 \cos^2\alpha_{\min}}\right\}}{M_{F0y}^2 C_{F0y}^2} \tag{21}$$

[34] The surface waves obtained in the high-Mach-number K-H instability can serve as localized disturbances that move supermagnetosonically with respect to the plasma in region 1 or 2. In our two-dimensional simulations, the surface disturbances are a series of line sources launching from the ridges of the surface waves as shown in Figure 9.

[35] Figure 9 is a three-dimensional sketch of nonlinear plane waves generated by a supermagnetosonic flow over a surface wave. This sketch is for $(U_t - V_{0y1})^2 \geq C_{F0y1}^2$ and $(U_t - V_{0y2})^2 > C_{F0y2}^2$. We try to show that the flaring angles (α_1 and α_2) of the nonlinear plane waves can be explained based on the Mach angle of the fast magnetosonic wedges generated by a series of line source in MHD plasma. The Mach angle of the fast magnetosonic wedges depends on the Mach number, orientation of the ambient magnetic field, and plasma beta of the background medium.

[36] Let θ_0 be the angle between the ambient magnetic field and the y-axis. For $\theta_0 = 0°$, the Mach angle α of the fast magnetosonic wedges is the same as the one obtained in equation (19). For $\theta_0 = 90°$, the Mach angle α of the fast magnetosonic wedges is the same as the $\alpha_{\max}$ obtained in equation (20). For any given θ_0, the Mach angle of the fast magnetosonic wedges can be determined from the sketch shown in Figure 10.

[37] Figure 10 shows how to determine the Mach angle α of the fast magnetosonic wedges for any given θ_0. Let us consider a line-type disturbance moving toward the $-y$ direction with speed $V_S = M_{F0y}C_{F0y}$ relative to the background medium. Following the same arguments as dis-

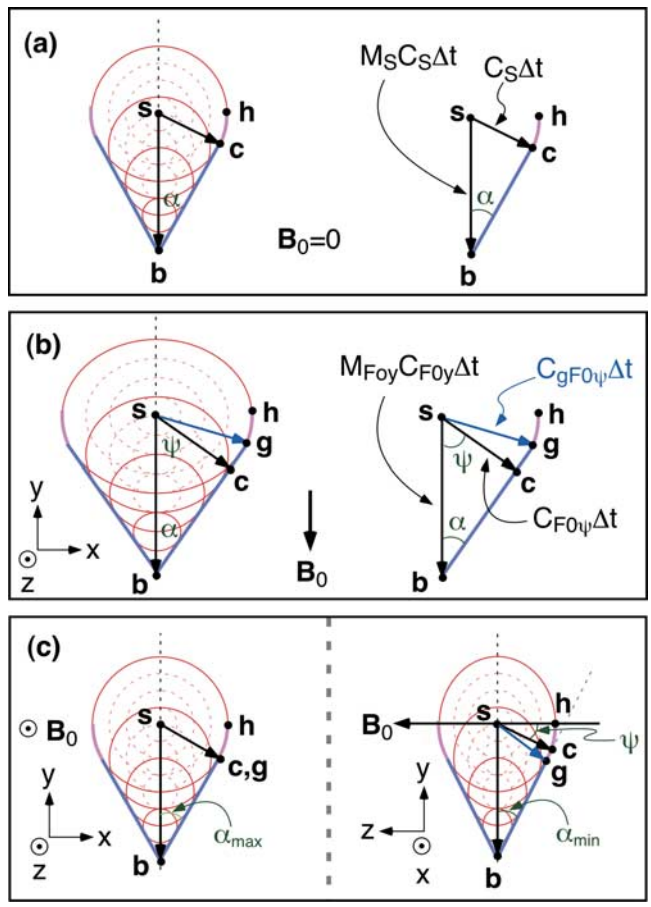

Figure 8. Sketches of formation of sonic/magnetosonic Mach cone by a point-source disturbance, which moves supersonic/supermagnetosonic with respect to the background medium. See the text for the detail discussion on how to determine the Mach angle α of the sonic Mach cone.

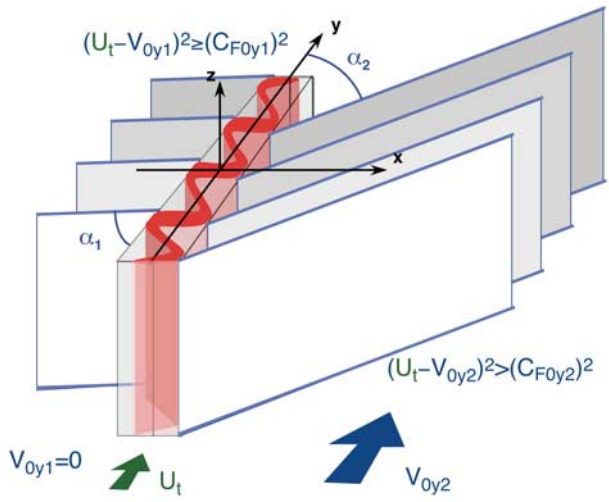

Figure 9. Sketch of three-dimensional distribution of plane waves and surface wave found in our simulation of high-Mach-number K-H instability. The flaring angles α_1 and α_2 of the nonlinear waves on two sides of the surface wave will be used to compare with the predicted Mach angles in Figure 11.

cussed in Figure 8b, we have $sb = V_S\Delta t = M_{F0y}C_{F0y}\Delta t$ and $sc = C_{F0\psi}\Delta t$, where $C_{F0\psi}$ is the phase speed of fast mode wave that propagates along the plane wave normal direction (**n**), and C_{F0y} is the phase speed of fast mode wave that propagates along the surface wave direction (**y**). Namely,

$$C_{F0\psi}^2 = \frac{1}{2}\left\{C_{A0}^2 + C_{S0}^2 \cdot + \sqrt{\left(C_{A0}^2 + C_{S0}^2\right)^2 - 4C_{A0}^2 C_{S0}^2 \cos^2\psi}\right\} \quad (22)$$

$$C_{F0y}^2 = \frac{1}{2}\left\{C_{A0}^2 + C_{S0}^2 \cdot + \sqrt{\left(C_{A0}^2 + C_{S0}^2\right)^2 - 4C_{A0}^2 C_{S0}^2 \cos^2\theta_0}\right\}, \quad (23)$$

where $C_{S0}^2 = 5p_0/3\rho_0$ and $C_{A0}^2 = B_0^2/\mu_0\rho_0$.

[38] Since vector *sc* in Figure 10 is normal to the surface of plane wave and since points *a*, *b*, *c*, and *d* are on the surface of plane wave, we can obtain the following relations:

$$\cos\psi = \frac{sc}{as} = \frac{sb\cdot\sin\alpha}{as} = \frac{(as\cdot\cos\theta_0)\cdot\sin\alpha}{as} = \cos\theta_0\sin\alpha \quad (24)$$

$$\sin\alpha = \frac{sc}{sb} = \frac{C_{F0\psi}}{M_{F0y}C_{F0y}}, \quad (25)$$

where $C_{F0\psi}$ and C_{F0y} are given in equations (22) and (23), respectively.

[39] Substituting equation (24) into equation (22) then substituting the resulting equation and the equation (23) into the equation (25) to solve for $\sin^2\alpha$, it yields

$$\sin^2\alpha = \frac{C_{S0}^2 + C_{A0}^2}{M_{F0y}^2 C_{F0y}^2} - \frac{C_{S0}^2 C_{A0}^2\cos^2\theta_0}{M_{F0y}^4 C_{F0y}^4}. \quad (26)$$

For $M_{F0y} \geq 1$, equation (26) yields

$$\alpha = \sin^{-1}\sqrt{\frac{C_{S0}^2 + C_{A0}^2}{M_{F0y}^2 C_{F0y}^2} - \frac{C_{S0}^2 C_{A0}^2\cos^2\theta_0}{M_{F0y}^4 C_{F0y}^4}}. \quad (27)$$

[40] Let β_0 be the ratio between the thermal pressure p_0 and the magnetic pressure $B_0^2/2\mu_0$. We have $C_{S0}^2/C_{A0}^2 = \gamma\beta_0/2$, where $\gamma = 5/3$. Equation (27) can be rewritten as

$$\alpha = \sin^{-1}\sqrt{\frac{(\gamma\beta_0/2)+1}{M_{F0y}^2\left(C_{F0y}^2/C_{A0}^2\right)} - \frac{(\gamma\beta_0/2)\cos^2\theta_0}{M_{F0y}^4\left(C_{F0y}^2/C_{A0}^2\right)^2}}, \quad (28)$$

where

$$\frac{C_{F0y}^2}{C_{A0}^2} = \frac{1}{2}\left\{1 + \frac{\gamma\beta_0}{2} + \sqrt{\left(1+\frac{\gamma\beta_0}{2}\right)^2 - 2\gamma\beta_0\cos^2\theta_0}\right\}. \quad (29)$$

[41] As we can see that the Mach angle α given in equation (28) is a function of M_{F0y}, θ_0, and β_0.

[42] Figure 11 shows the theoretical solutions of the Mach angle α as a function of M_{F0y} for a given plasma beta $\beta_0 = 0.5$ and for three different θ_0 (i.e., $\theta_0 = 0°$, 60°, and 90°). It can be seen that the Mach angle α decreases with increasing Mach number M_{F0y} or increasing θ_0. The symbols shown in Figure 11 are the measured flaring angles of the nonlinear plane waves in the simulation with the corresponding plasma beta ($\beta_0 = 0.5$), Mach number M_{F0y},

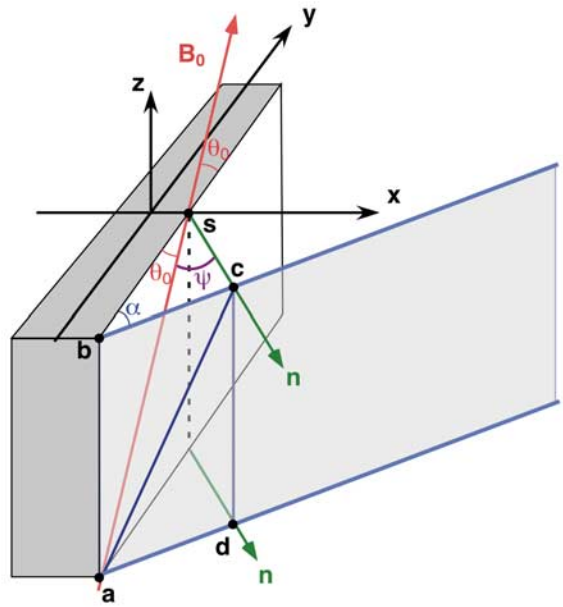

Figure 10. Illustration of the relation among the three angles α, θ_0, and ψ, where α is the Mach angle, θ_0 is the acute angle between the surface wave propagation direction and the background magnetic field direction, and ψ is the acute angle between the plane wave propagation direction and the background magnetic field direction. See the text for the detail discussion on how to determine Mach angle α.

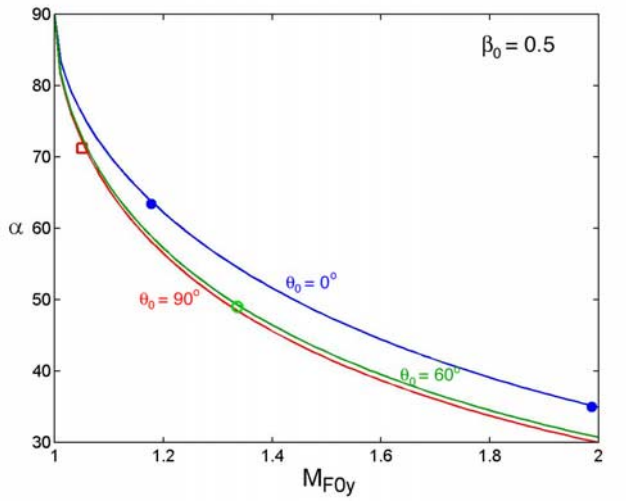

Figure 11. Comparison of the Mach angles derived in the calculation and obtained in the simulation. Theoretical solutions of the Mach angle α as a function of M_{F0y} for a given plasma beta $\beta_0 = 0.5$, and for three different θ_0 (i.e., $\theta_0 = 0°$, 60°, and 90°). The symbols shown in this figure are the flaring angles of the nonlinear plane waves measured from simulation results with the corresponding plasma beta ($\beta_0 = 0.5$), Mach number M_{F0y}, and θ_0, where the two solid circles are for $\theta_0 = 0°$, the open circle is for $\theta_0 = 60°$, and the open square is for $\theta_0 = 90°$. The flaring angles measured from our simulation results (the color-coded symbols) are in good agreement with the predicted Mach angles (the color-coded curves) obtained from equation (28).

and θ_0. The two solid circles are for $\theta_0 = 0°$, the open circle is for $\theta_0 = 60°$, and the open square is for $\theta_0 = 90°$. As we can see that the flaring angles measured from our simulation results (the color-coded symbols) are in good agreement with the predicted Mach angles (the color-coded curves) obtained from equation (28). To further verify the proposed model, we check wave characteristics of the nonlinear waves found in high-Mach-number simulations.

[43] Figure 12 shows the spatial profiles of the normalized plasma density (ρ/ρ_a) and the normalized magnetic field strength (B/B_a) along the y direction obtained in Case 3 at three fixed x locations (a) $x = -7.5W$ (in region 1), (b) $x = 0$, and (c) $x = +7.5W$ (in region 2) at $t = 37.5\tau_a$. Since the variations of ρ and B are in-phase in both regions 1 and 2, the waves are nonlinear fast-mode waves.

[44] Figure 13 shows the spatial profiles of the normalized plasma density (ρ/ρ_a) and the normalized magnetic field strength (B/B_a) along the y direction obtained in Case 4 at three fixed x locations $x = -2.5W$ (in region 1) (Figure 13a), $x = 0$ (Figure 13b), and $x = +10W$ (in region 2) (Figure 13c) at $t = 75\tau_a$. The variations of ρ and B are in-phase in region 2 but nearly out-of-phase in region 1 and at $x = 0$. Again, the nonlinear plane waves in the high-Mach-number region (region 2) are predominately nonlinear fast-mode waves. Nonlinear slow-mode waves are found in region 1 but very close to the velocity-shear layer. The slow-mode Mach numbers of the surface waves are greater than 1 in all the cases shown in Table 1. Since our simulation is two-dimensional and the group velocity of the slow-mode wave is nearly field-aligned, the slow-mode nonlinear waves generated by the surface waves cannot be seen if $\theta_0 = 90°$. Thus the slow-mode waves can be seen in Figure 13, where the background magnetic field is along the y direction, but not in Figure 12, where the background magnetic

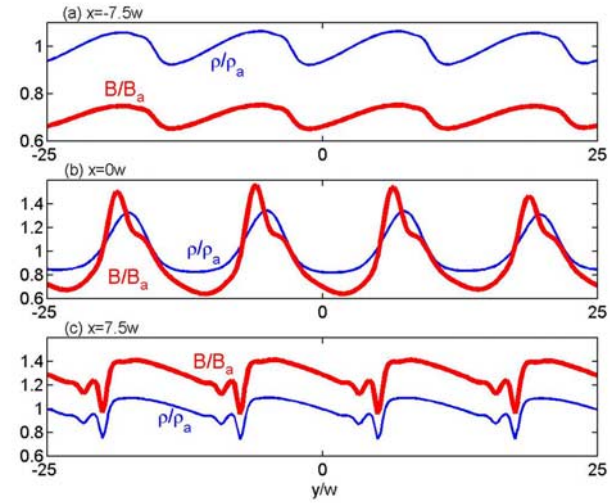

Figure 12. Spatial profiles of the normalized plasma density (ρ/ρ_a) and the normalized magnetic field strength (B/B_a) along the y direction obtained in Case 3 at three fixed x locations (a) $x = -7.5W$ (in region 1), (b) $x = 0$, and (c) $x = +7.5W$ (in region 2) at $t = 37.5\tau_a$. Since the variations of ρ and B are in-phase in both regions 1 and 2, the waves in both regions are nonlinear fast-mode waves.

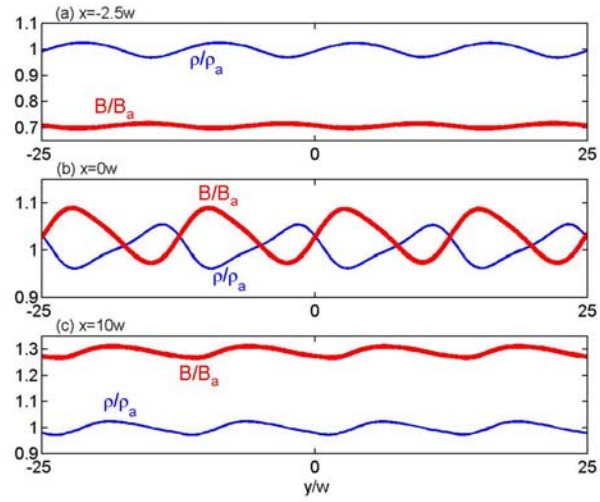

Figure 13. Spatial profiles of the normalized plasma density (ρ/ρ_a) and the normalized magnetic field strength (B/B_a) along the y direction obtained in Case 4 at three fixed x locations (a) $x = -2.5W$ (in region 1), (b) $x = 0$, and (c) $x = +10W$ (in region 2) at $t = 75\tau_a$. The variations of ρ and B are in-phase in region 2 but nearly out-of-phase in region 1 and at $x = 0$.

field is along the z direction. Development of a slow rarefaction layer near the velocity shear region has also been reported in previous simulations of K-H instability [e.g., *Miura*, 1982, 1984].

[45] *Miura* [1990, 1992] studied the K-H instability at the flanks of the magnetopause, in which the interplanetary magnetic field (IMF) is assumed to be parallel or antiparallel to the magnetosheath flow. He employed the Alfvén Mach number and the sonic Mach number to classify his simulation results. He found a shock structure in his simulations when the sonic Mach number is large enough. He concluded that the shock structure is an MHD parallel shock. He showed that the parallel shock structure obtained in his simulation satisfies the Rankine-Hugoniot (R-H) jump condition of a gas dynamic shock with Mach number equal to 1.29, regardless the fact that the effect of magnetic field jump should not be ignored in low-Mach-number parallel shock with Mach number less than 2 [*Kantrowitz and Petschek*, 1996].

[46] In contrast, we employed two fast-mode Mach numbers, M_{F0y1} and M_{F0y2}, to classify our simulation results and use a longer simulation system extending further away from the TD surface. The extended system allows the fully development of the nonlinear plane waves that might occur in the high-Mach-number cases and allows us to measure the flaring angles of these nonlinear plane waves more accurately. We found that the flaring angles of these nonlinear plane waves are in good agreement with the theoretical prediction, in which the plane wave is assumed to propagate at the fast-mode speed $C_{F0\psi}$. Namely, these nonlinear plane waves found in the high-Mach number cases are nonlinear waves with fast magnetosonic Mach number equal to one but not greater than one.

[47] Since there are no uniform states on upstream and downstream sides of the nonlinear plane waves and since the MHD R-H jump conditions are constructed based on uniform boundary conditions [*Kantrowitz and Petschek*, 1996; *Chao and Goldstein*, 1972], it is difficult to examine weather these nonlinear waves are shock waves or not by comparing our simulation results with the MHD R-H jump conditions. However, if these plane waves were shock waves, the flaring angle of these shock waves should be greater than the one estimated by equation (28). It would be inconsistent with the results shown in Figure 11. Moreover, since the plasma flow in the downstream of a fast shock is submagnetosonic, it would be impossible to find another fast shock in the downstream region with the same propagation speed as the proceeding shock. Thus we conclude that no matter how fast the flow moves relative to the surface wave, the nonlinear plane waves found in the high-Mach number cases are not shocks but soliton-like blast waves as suggested by J. K. Chao (private communication, 2004).

[48] Indeed, without sufficient dissipations, the shock waves cannot be formed in an ideal MHD simulation. The non-MHD effects, including dispersion effect, due to finite-ion-inertial-length effect, and dissipation effect, due to wave-particle interactions, can affect the structures of the nonlinear fast-mode plane waves. If the dispersion effect due to finite ion inertial length is included, the nonlinear fast-mode plane waves with $0 \ll \theta_0 \ll 90^\circ$ may turn into two-fluid fast-mode solitons [e.g., *Lyu and Kan*, 1989] with whistler precursors upstream from the solitons. A two-fluid simulation can easily verify this prediction. On the other hand, kinetic simulation, which has better control on the dissipation mechanism, is more suitable for study whether these soliton-like nonlinear plane waves can develop into fast shocks or not.

5. Summary and Discussion

[49] In summary, we study Kelvin-Helmholtz instabilities in this paper by means of two-dimensional MHD simulations with an extremely long dimension along the direction normal to the velocity-shear layer. Our simulation results indicate that the nonlinear evolution of surface waves at a TD depends on the fast-mode Mach numbers of the plasma flows on two sides of the TD in the surface wave rest frame. When the fast-mode Mach numbers on both sides of the TD are less than 1, the K-H instability can grow into vortices or kink-type surface waves, depending on the orientation of the ambient magnetic field. When the fast-mode Mach number on either side of the TD is greater than 1, nonlinear fast-mode plane waves are developed from the ridges of the surface waves and extended into the region distant from the TD. A theoretical model based on the formation of the fast magnetosonic Mach cone and the fast magnetosonic wedge is proposed to explain the formation of these nonlinear plane waves. The Mach angle of the fast magnetosonic wedge is derived as a function of the Mach number, the orientation of ambient magnetic field, and the plasma beta of the background medium. The flaring angles of these nonlinear plane waves measured from our simulation results are in good agreement with the Mach angles predicted by the theoretical model. We propose that the generation and propagation of the nonlinear fast-mode plane waves can provide a mechanism for steady and efficient momentum and energy transferring across a TD in the events of K-H instability as predicted by *Pu and Kivelson* [1983]. A comprehensive analysis of the momentum and energy transports in the events of K-H instability will be presented elsewhere in the near future.

5.1. Application to the Earth's Magnetopause

[50] Applications of our simulation results to the magnetopause are discussed below. If the solar wind speed is fast enough, nonlinear plane waves can form at the flanks of the magnetosheath during northward IMF. According to the gas dynamic magnetosheath flow model by *Spreiter et al.* [1966], the plasma flow near the subsolar region is subsonic and become supersonic toward the flanks. Thus during the period of high-speed solar wind, the speed of magnetosheath flow can easily reach twice the fast mode speed in the flanks of the magnetosheath. Nonlinear fast-mode mode waves can be generated by the surface wave disturbances at the magnetopause. The propagation direction of the fast-mode waves in the magnetosheath is sunward but these waves are blown back by the antisunward flow in the magnetosheath. Note that if finite dissipation is included, parallel shocks are expected to form at the flank of magnetopause when IMF is parallel or antiparallel to the solar wind direction as proposed by *Miura* [1992].

[51] Figure 14 is a sketch of K-H instabilities occurring at the Earth's magnetopause on the equatorial plane during

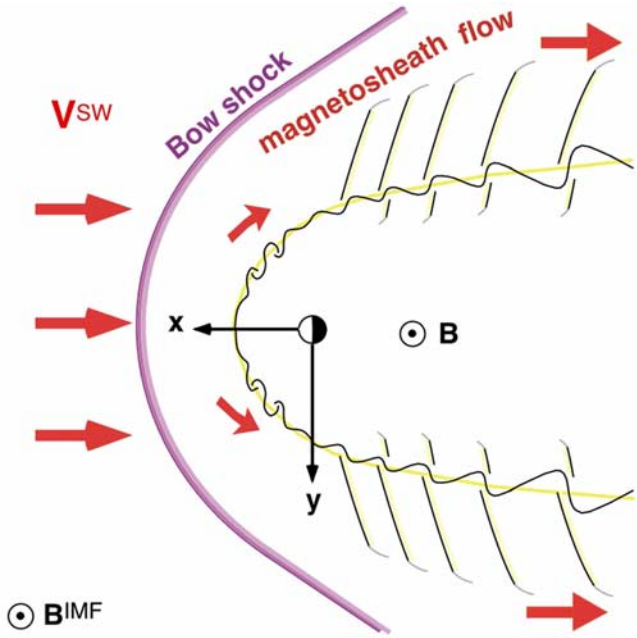

Figure 14. A sketch to illustrate the K-H instabilities at the dawn and dusk magnetopause and in the low-latitude boundary layer (LLBL) during periods of northward IMF and when the flank magnetosheath flow speed is fast enough such that the surface waves at flank magnetopause move at a speed faster than the fast-mode speed in the plasma sheet.

northward IMF and when the magnetosheath flow speed is fast enough such that the surface waves move at a speed faster than the fast-mode speed in the plasma sheet. The wavy structure at the flank magnetopause sketched in Figure 14 and the profiles of the nonlinear waves shown in Figure 12 are similar to the nonsinusoidal wave structures observed by *Chen and Kivelson* [1993]. The extensions of the nonlinear plane waves (lighter traces) extended continuously away from the tips of the nonlinear plane waves in Figure 14 are commonly found in our simulation results. They are the nonlinear waves associated with the arc *hg* shown in Figure 8. Note that a similar but different sketch can be found in the paper by *Miura* [1995], in which shocklet structures are formed in the magnetosheath side of the magnetopause, but the surface wave is still characterized by antisunward steepening due to presence of vortex structures inside the magnetopause.

[52] When the IMF is southward, the magnetic reconnection at the dayside magnetopause can generate high-speed jet streams flowing along the magnetopause. The jet streams can also result in K-H instability and generate nonlinear plane waves on two sides of the magnetopause.

[53] Figure 15 shows a sketch of the K-H instability occurring at the magnetopause in the noon-midnight meridian plane during southward IMF. The lower panel shows an example of simulation results of the K-H instabilities generated by a super-magnetosonic jet steam at the center of the transition layer of a TD. The super-magnetosonic jet stream can result in pairs of nonlinear fast-mode waves, which are similar to the nonlinear waves found in the laboratory experiment by *Papamoschou and Roshko* [1988]. Owing to the nonuniform distribution of the magnetic field and the plasma density along the noon-midnight meridian plane, the structures of the nonlinear waves in the magnetospheric boundary could be much more complicated than the one sketched in the top panel of Figure 15.

5.2. Non-MHD Effects Associated With the K-H Instability

[54] The microscopic structures of the vortices, kink-type surface waves, and nonlinear plane waves cannot be fully described by the MHD simulations. The dispersion effects due to finite ion inertial length can be included by a Hall-MHD model [e.g., *Chacon et al.*, 2003] or by an ion-electron two-fluid plasma model, in which the finite

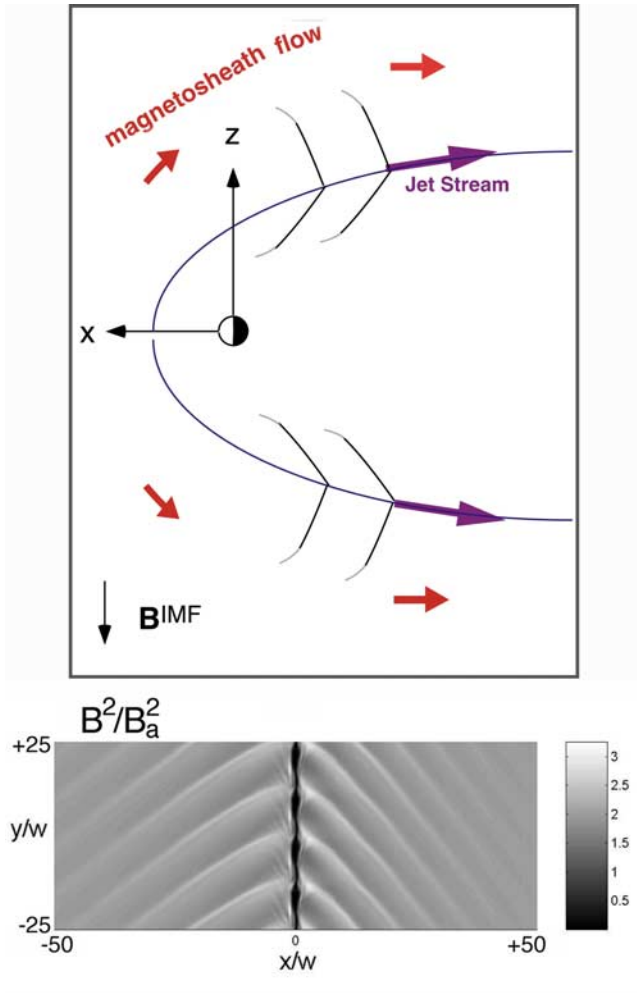

Figure 15. A sketch to illustrate the K-H instabilities at the magnetopause in the noon-midnight meridian plane during southward IMF (the top panel) and an example of simulation results of the K-H instabilities generated by a super-magnetosonic jet steam at the center of the transition layer of a TD (the lower panel). When the IMF is southward, the magnetic reconnection at the dayside magnetopause can generate high-speed jet streams flowing along the magnetopause. The jet streams can also result in K-H instability and generate nonlinear plane waves on two sides of the magnetopause. See the text for detail discussion.

electron inertial effect can also be included [e.g., *Nakamura et al.*, 2004]. The kinetic effects due to finite ion gyroradius are included in hybrid simulation. Results of the ion kinetic effects have been demonstrated in previous hybrid simulation studies of vortex-type K-H instability [e.g., *Thomas and Winske*, 1993; *Thomas*, 1995], quasi-perpendicular shocks [e.g., *Leroy et al.*, 1982], and quasi-parallel shocks [e.g., *Lyu and Kan*, 1993, and references therein]. We believe that the dispersion effects, the kinetic effects, and wave-wave interference effects all play important roles in the event of K-H instability in space plasma. For example, the whistler waves are expected to exist as a precursor of the nonlinear plane waves in Case 4 and in Figure 15 if the dispersion effect is included. Thus the whistler waves observed near a reconnection site [e.g., *Deng and Matsumoto*, 2001] might be a cause as well as a consequence of the magnetic reconnection and the K-H instability. In addition to the whistler waves, the slow-mode and the intermediate-mode nonlinear waves including rotational discontinuities, intermediate shocks, and slow shocks may be formed along the velocity shear layer under the similar processes as the formation of the nonlinear fast-mode plane waves discussed in this paper. Rotational discontinuities are commonly observed at the leading edge and trailing edge of high-speed solar wind where the velocity shear occurs [e.g., *Belcher and Davis*, 1971; *Neugebauer and Buti*, 1990]. Intermediate shock has been observed near a tangential discontinuity in the solar wind with shock normal perpendicular to the normal of tangential discontinuity [*Chao et al.*, 1993]. Thus the velocity shear regions in the solar wind are likely to be the source regions of slow shocks, intermediate shocks, and rotational discontinuities. Indeed, we believe that the simulation results of the high-Mach-number K-H instabilities obtained in this study provide useful information on the locations where the low-Mach-number shocks and the two-fluid solitary waves [e.g., *Lyu and Kan*, 1989] might be found in the solar wind and in the magnetosphere.

[55] **Acknowledgments.** We would like to thank J. K. Chao for valuable comments and helpful discussions. This work is supported by NSC grants 92-2111-M-008-013, 92-2111-M-008-014, 93-2111-M-008-012, and 93-2111-M-008-003 to the National Central University.

[56] Shadia Rifai Habbal thanks Sheng-Hsien Chen and another referee for their assistance in evaluating this paper.

References

Belcher, J. W., and L. Davis Jr. (1971), Large-amplitude Alfvenic waves in the interplanetary medium, *J. Geophys. Res.*, *76*, 3534.

Chacon, L., D. A. Knoll, and J. M. Finn (2003), Hall MHD effects on the 2D Kelvin-Helmholtz/tearing instability, *Phys. Lett. A*, *308*, 187.

Chandrasekhar, S. (1961), *Hydrodynamic and Hydromagnetic Stability*, Oxford Univ. Press, New York.

Chao, J. K., and B. Goldstein (1972), Modification of the Rankine-Hugoniot relations for shocks in space, *J. Geophys. Res.*, *77*, 5455.

Chao, J. K., L. H. Lyu, B. H. Wu, A. J. Lazarus, T. S. Chang, and R. P. Lepping (1993), Observations of an intermediate shock in interplanetary space, *J. Geophys. Res.*, *98*, 17,443.

Chen, S. H., and M. G. Kivelson (1993), On nonsinusoidal waves at the Earth's magnetopause, *Geophys. Res. Lett.*, *20*, 2699.

Chen, S. H., M. G. Kivelson, J. T. Gosling, R. J. Walker, and A. J. Lazarus (1993), Anomalous aspects of magnetosheath flow and of the shape and oscillations of the magnetopause during an interval of strongly northward interplanetary magnetic field, *J. Geophys. Res.*, *98*, 5727.

Deng, X. H., and H. Matsumoto (2001), Rapid magnetic reconnection in the Earth's magnetosphere mediated by whistler waves, *Nature*, *410*, 557.

Fairfield, D. H., A. Otto, T. Mukai, S. Kokubun, R. P. Lepping, J. T. Steinberg, A. J. Lazarus, and T. Yamamoto (2000), Geotail observations of the Kelvin-Helmholtz instability at the equatorial magnetotail boundary for parallel northward fields, *J. Geophys. Res.*, *105*, 21,159.

Fairfield, D. H., C. J. Farrugia, T. Mukai, T. Nagai, and A. Federov (2003), Motion of the dusk flank boundary layer caused by solar wind pressure changes and the Kelvin-Helmholtz instability: 10–11 January 1997, *J. Geophys. Res.*, *108*(A12), 1460, doi:10.1029/2003JA010134.

Kantrowitz, A., and H. E. Petschek (1996), MHD characteristics and shock waves, in *Plasma Physics in Theory and Application*, edited by W. B. Kunkel, p. 184, McGraw-Hill, New York.

Leroy, M. M., D. Winske, C. C. Goodrich, C. S. Wu, and K. Papadopoulos (1982), The structure of perpendicular bow shocks, *J. Geophys. Res.*, *87*, 5081.

Lyu, L. H., and J. R. Kan (1989), Nonlinear two-fluid hydromagnetic waves in the solar wind: Rotational discontinuity, soliton, and finite-extent Alfven wave train solutions, *J. Geophys. Res.*, *94*, 6523.

Lyu, L. H., and J. R. Kan (1993), Ion dynamics in high-Mach-number quasi-parallel shocks, *J. Geophys. Res.*, *98*, 985.

Manuel, J. R., and J. C. Samson (1993), The spatial development of the low-latitude boundary layer, *J. Geophys. Res.*, *98*, 17,367.

Mavromichalaki, H., X. Moussas, J. J. Quenby, J. F. Valdes-Galicia, E. J. Smith, and B. T. Thomas (1988), Relatively stable, large-amplitude Alfven waves seen at 2.5 and 5.0 AU, *Solar Phys.*, *116*, 337.

Miura, A. (1982), Nonlinear evolution of the magnetohydrodynamic Kelvin-Helmholtz instability, *Phys. Rev. Lett.*, *49*, 779.

Miura, A. (1984), Anomalous transport by magnetohydrodynamic Kelvin-Helmholtz instabilities in the solar wind-Magnetosphere interaction, *J. Geophys. Res.*, *89*, 801.

Miura, A. (1987), Simulation of Kelvin-Helmholtz instability at the magnetospheric boundary, *J. Geophys. Res.*, *92*, 3195.

Miura, A. (1990), Kelvin-Helmholtz instability for supersonic shear flow at the magnetospheric boundary, *Geophys. Res. Lett.*, *17*, 749.

Miura, A. (1992), Kelvin-Helmholtz instability at the magnetospheric boundary: Dependence on the magnetosheath sonic Mach number, *J. Geophys. Res.*, *97*, 10,655.

Miura, A. (1995), Kelvin-Helmholtz instability at the magnetopause: Computer simulations, in *Physics of the Magnetopause*, *Geophys. Monogr. Ser.*, vol. 90, edited by P. Song, B. U. Ö. Sonnerup, and M. F. Thomsen, pp. 285–291, AGU, Washington, D. C.

Miura, A. (1997), Compressible magnetohydrodynamic Kelvin-Helmholtz instability with vortex pairing in two-dimensional transverse configuration, *Phys. Plasmas*, *4*, 2871.

Miura, A. (1999), Self-organization in the two-dimensional magnetohydrodynamic transverse Kelvin-Helmholtz instability, *J. Geophys. Res.*, *104*, 395.

Miura, A., and P. L. Pritchett (1982), Nonlocal stability analysis of the MHD Kelvin-Helmholtz instability in a compressible plasma, *J. Geophys. Res.*, *87*, 7431.

Nakamura, T. K., D. Hayashi, M. Fujimoto, and I. Shinohara (2004), Decay of the MHD-scale Kelvin-Helmholtz vortices mediated by parasitic electron dynamics, *Phys. Rev. Lett.*, *92*, 145001.

Neugebauer, M., and B. Buti (1990), A search for evidence of the evolution of rotational discontinuities in the solar wind from nonlinear Alfven waves, *J. Geophys. Res.*, *95*, 13.

Ogilvie, K. W., and R. J. Fitzenreiter (1989), The Kelvin-Helmholtz instability at the magnetopause and inner boundary layer surface, *J. Geophys. Res.*, *94*, 15,113.

Otto, A., and D. H. Fairfield (2000), Kelvin-Helmholtz instability at the magnetotail boundary: MHD simulation and comparison with Geotail observations, *J. Geophys. Res.*, *105*, 21,175.

Papamoschou, D., and A. Roshko (1988), The compressible turbulent shear layer: an experimental study, *J. Fluid Mech.*, *197*, 453.

Press, W. H., B. P. Flannery, S. A. Teukolsky, and W. T. Vetterling (1988), *Numerical Recipes*, Cambridge Univ. Press, New York.

Pu, Z. Y., and M. G. Kivelson (1983), Kelvin-Helmholtz instability at the magnetopause: Energy flux into the magnetopause, *J. Geophys. Res.*, *88*, 853.

Richtmyer, R. D., and K. W. Morton (1967), *Difference Methods for Initial-Value Problems*, 2nd ed., John Wiley, Hoboken, N. J.

Spreiter, J. R., A. L. Summers, and A. Y. Alksne (1966), Hydromagnetic flow around the magnetosphere, *Planet. Space Sci.*, *14*, 223.

Thomas, V. A. (1995), Kinetic simulation of Kelvin-Helmholtz instability in a finite sized jet, *J. Geophys. Res.*, *100*, 12,011.

Thomas, V. A., and D. Winske (1993), Kinetic simulations of the Kelvin-Helmholtz instability at the magnetopause, *J. Geophys. Res.*, *98*, 11,425.

Wu, C. C. (1986), Kelvin-Helmholtz instability at the magnetopause boundary, *J. Geophys. Res.*, *91*, 3042.

S. H. Lai and L. H. Lyu, Institute of Space Science, National Central University, Chung-Li, Taiwan 32001. (lyu@jupiter.ss.ncu.edu.tw)